

Shape-tunable wax microparticle synthesis via microfluidics and droplet impact

Doojin Lee,¹ Shilpa N. Beesabathuni,² and Amy Q. Shen^{1,a)}

¹*Micro/Bio/Nanofluidics Unit, Okinawa Institute of Science and Technology Graduate University, Okinawa, 904-0495 Japan*

²*Mechanical Engineering Department, University of Washington, Seattle, Washington 98195, USA*

(Received 19 August 2015; accepted 1 December 2015; published online 15 December 2015)

Spherical and non-spherical wax microparticles are generated by employing a facile two-step droplet microfluidic process which consists of the formation of molten wax microdroplets in a flow-focusing microchannel and their subsequent off-chip crystallization and deformation via microdroplet impingement on an immiscible liquid interface. Key parameters on the formation of molten wax microdroplets in a microfluidic channel are the viscosity of the molten wax and the interfacial tension between the dispersed and continuous fluids. A cursory phase diagram of wax morphology transition is depicted depending on the Capillary number and the Stefan number during the impact process. A combination of numerical simulation and analytical modeling is carried out to understand the physics underlying the deformation and crystallization process of the molten wax. The deformation of wax microdroplets is dominated by the viscous and thermal effects rather than the gravitational and buoyancy effects. Non-isothermal crystallization kinetics of the wax illustrates the time dependent thermal effects on the droplet deformation and crystallization. The work presented here will benefit those interested in the design and production criteria of soft non-spherical particles (i.e., alginate gels, wax, and polymer particles) with the aid of time and temperature mediated solidification and off-chip crosslinking. © 2015 AIP Publishing LLC.

[<http://dx.doi.org/10.1063/1.4937897>]

I. INTRODUCTION

Microfluidics has become an emerging and versatile tool to synthesize particles and droplets, providing fine control over the size and shape,^{1–5} chemical functionality and anisotropy,^{6,7} porosity,⁸ and internal structure^{9–11} of particles. In particular, microfluidic-assisted techniques can tailor-design particles with unique sizes and shapes that are difficult to achieve by using conventional techniques such as template molding,^{12,13} seeded emulsion polymerization,¹⁴ self-assembly of colloids through liquid protrusions,¹⁵ and stretching of soft spherical particles.^{16,17} In this regard, microfluidic techniques are highly desirable to generate particles with homogeneous morphologies and monodispersed sizes due to their consistent and reproducible behavior.

A number of recent studies explored the production and use of non-spherical particles in biotechnology,^{18,19} cosmetics,²⁰ pharmaceutical,^{21,22} optics,^{23,24} and image enhancement.²⁵ Non-spherical particles are remarkably applicable in a variety of applications for their unique properties such as anisotropic responses to external fields,^{26–28} large surface areas,²⁹ and high packing density.³⁰ Many groups have successfully synthesized non-spherical microgels and polymeric particles by using microfluidic platforms and utilizing ultraviolet, crosslinking, polymerization, and thermal energy to solidify particles *in-situ*. An external crosslinking technique after impinging on liquid drops in solutions also provided new opportunities to produce particles with various anisotropic dimensions. Hu and coworkers, for instance, demonstrated a

^{a)} Author to whom correspondence should be addressed. Electronic mail: amy.shen@oist.jp

simple strategy to prepare non-spherical alginate particles with various morphologies by using droplet microfluidics, combined with an external ionic crosslinking procedure.³¹ This unique external crosslinking step gives additional experimental parameters for tailored control of the particle morphology, e.g., viscosity of the bath liquid, releasing height of the drop, as well as the flow rate ratio in the microchannel.^{31,32}

Wax based materials have been widely used in dentistry,³³ food processing,³⁴ cosmetics,²⁰ and pharmaceutical applications³⁵ since they are abundant in nature, biocompatible, and facile to the use of encapsulation of active compounds and ingredients. We recently demonstrated that millimeter size molten wax drops could be solidified into particles with mushroom, ellipsoid, disc, and flake-like morphologies upon striking an immiscible liquid interface.³⁶ We investigated the deformation and solidification of molten wax drops upon impacting an immiscible liquid by varying the initial temperature and viscoelasticity of the molten drop, drop size, impact velocity, viscosity and temperature of the bath fluids, and the interfacial tension between the molten wax and bath fluid. However, it is more difficult to generate micron size non-spherical wax particles in comparison to millimeter size non-spherical wax particles since the inertial effect of the wax microdroplets is much smaller than that of the millimeter sized wax drops. A thorough understanding of the mechanism of controllable droplet generation in a microfluidic platform, deformation and crystallization of the molten wax drop due to liquid-liquid impact can shed insights on key factors to control tailored sizes and morphologies of the wax particles.

In this study, we propose a two-step method by utilizing a microfluidic platform to produce size-controllable molten wax microdroplets in a flow-focusing channel, followed by subsequent deformation and solidification processes during liquid-liquid impact in an aqueous bath solution to generate non-spherical wax microparticles (see schematics in Figure 1). Through systematic experiments we build the phase diagram of final morphologies of wax particles with respect to the Capillary number and the Stefan number. A simplified analytical model is proposed to understand dominant factors on the droplet deformation process. Numerical simulation by coupling heat transfer and crystallization kinetics processes is performed to investigate the droplet solidification. This strategy not only provides experimental and theoretical evidences for the deformation process but also presents design and production criteria of soft non-spherical particles (i.e., alginate gels, wax, and polymer particles) with the aid of time and temperature mediated solidification and off-chip crosslinking.

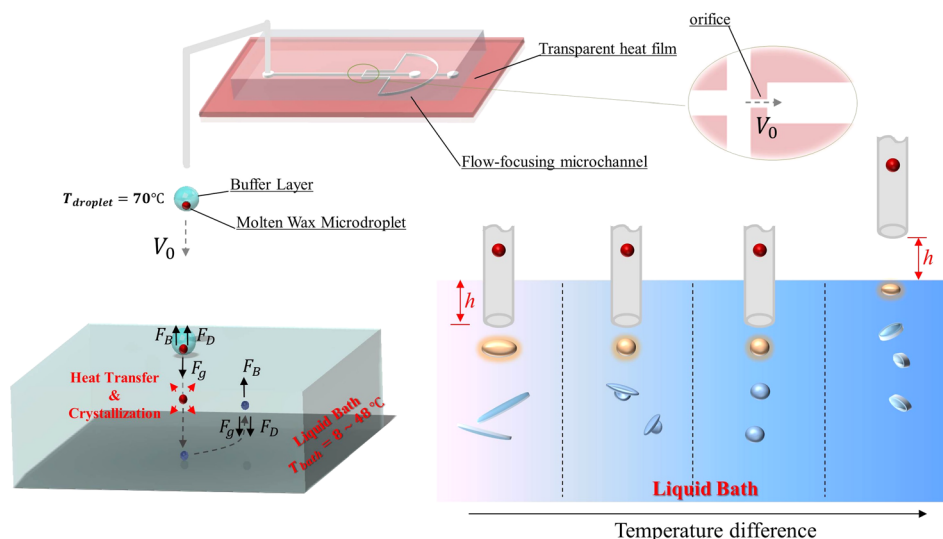


FIG. 1. Schematics of the experimental setup of molten wax droplet impacting a cooling aqueous medium.

II. BACKGROUND

An early study for the emulsion droplet production in a flow-focusing microchannel showed the droplet size dependence as a function of the flow rate and flow rate ratio.¹ The geometric effect (i.e., the width and depth of the channel) was also investigated to determine the droplet size in T-junction microchannels, showing an increase in the size of droplets with increasing depth of the channel.^{37,38} In most cases, Capillary number is considered as a key dimensionless parameter to determine the droplet production,

$$Ca = \frac{\eta_0 V_0}{\sigma_i} = \frac{\text{Viscous Force}}{\text{Interfacial Force}}, \quad (1)$$

where η_0 is the viscosity of the continuous phase or bath liquid, V_0 is the average velocity at the orifice of a microchannel (Figure 1), and σ_i is the interfacial tension between the dispersed and continuous phases.⁴² Consequently, the temperature dependent interfacial tension and viscosity of the liquid become important in thermally mediated droplet formation and breakup.^{39–41}

Extensive studies have investigated the deformation of drops upon impacting an immiscible liquid.^{43,44} During impact the viscous and elastic components of the bath fluid dictate the amount of energy dissipated and stored, respectively. Waigh *et al.* reported the deformation and process conditions of millimeter sized viscoelastic drops after impinging on a liquid interface in which dimensionless numbers (i.e., Weber, Reynolds, and Froude numbers) were used to describe the deformation behavior of viscoelastic drops.⁴⁵ We recently studied the deformation and solidification of millimeter sized wax drops upon impact at an immiscible liquid interface.³⁶ Dimensionless numbers such as the Weber, Reynolds, Capillary, and Stefan numbers were identified to be important to the deformation, solidification, and final morphology of wax particles. Besides the Capillary number and Stefan number, the Ohnesorge and Bond numbers are introduced to investigate the viscous, gravitational, and buoyancy effects, which can be used to characterize the deformation of wax microdroplets upon impact and subsequent droplet migration in the bath liquid. The Fourier number (important for unsteady state conduction-convection problems) is used to examine the crystallization behavior of the molten wax microdroplets. These dimensionless numbers are defined as

$$St = \frac{C_p \Delta T}{L_p} = \frac{\text{Sensible Heat}}{\text{Latent Heat}}, \quad (2)$$

$$Oh = \frac{\nu \rho_b}{(\rho_b D \sigma_i)^{1/2}} = \frac{\text{Viscous Force}}{\text{Inertial and Interfacial Forces}}, \quad (3)$$

$$Bo = \frac{(\rho_b - \rho_p) g D^2}{4 \sigma_i} = \frac{\text{Buoyancy and Gravity Forces}}{\text{Interfacial Force}}, \quad (4)$$

$$Fo = \frac{\alpha t}{D^2} = \frac{\text{Heat Conduction Rate}}{\text{Thermal Energy Storage Rate}}, \quad (5)$$

where C_p , ΔT , L_p , ν , ρ_b , D , σ_i , ρ_p , g , α , and t denote the specific heat of the bath liquid, temperature difference between the bath liquid and molten wax, latent heat of wax, kinematic viscosity of the bath liquid, density of the bath liquid, diameter of the molten wax droplet, interfacial tension between the molten wax and the bath liquid, density of the molten wax, gravity, thermal diffusivity of the molten wax, and elapsed time during the crystallization, respectively.

III. EXPERIMENTS

A. Materials

Vaseline, hexadecane, glycerol, and surfactant sodium dodecyl sulfate (SDS) were purchased from Sigma-Aldrich and used without further purification. The wax sample was prepared

TABLE I. Physical properties of the bath fluids at various temperatures.^a

Weight percent of glycerol [wt. %]	Density [Kg/m ³] and viscosity [Pa s]											
	8 °C		25 °C		32 °C		37 °C		43 °C		48 °C	
	ρ	η	ρ	η	ρ	η	ρ	η	ρ	η	ρ	η
0	999.81	0.0014	996.85	0.0009	994.86	0.0008	993.21	0.0007	990.98	0.0006	988.92	0.0006
20	1065.4	0.0029	1060.2	0.0017	1057.5	0.0014	1055.4	0.0013	1052.8	0.0011	1050.4	0.0010
40	1124.6	0.0078	1117.5	0.0041	1114.2	0.0032	1111.8	0.0028	1108.7	0.0024	1106.1	0.0021
60	1178.2	0.0304	1169.6	0.0128	1165.8	0.0095	1163.0	0.0079	1159.7	0.0063	1156.8	0.0054
80	1227.1	0.2193	1217.1	0.0669	1212.9	0.0446	1209.9	0.0342	1206.2	0.0255	1203.1	0.0203

^aThe densities and viscosities of aqueous glycerol solutions are calculated from the formula for a glycerol-water mixture⁴⁶ and verified by our measurements.

by mixing 80 wt. % Vaseline and 20 wt. % hexadecane, and stored at room temperature. The aqueous solutions of the bath fluid consist of different amount of glycerol (0, 20, 40, 60, and 80 wt. %) mixed with deionized (DI) water and 0.025 wt. % SDS. The density and viscosity of the aqueous glycerol solutions were obtained from the formula for a glycerol-water mixture (Table I).⁴⁶

The heat capacity, thermal conductivity, enthalpy of crystallization, and phase transition temperature of the wax sample were measured by using a differential scanning calorimeter (Auto Q20, TA instruments) (Table II). The molten wax sample changes its phase from liquid to crystallized wax when temperature decreases to its phase transition temperature ($\sim 45.93^\circ\text{C}$). The dynamic viscosity of the wax sample at a shear rate 1000 s^{-1} was measured to be from 0.083 to 0.007 Pa s at a fixed temperature ranging from 40°C to 80°C , by using a strain-controlled rheometer (ARES-G2, TA instruments) with a steel cone-plate geometry (50 mm in diameter and 1° truncation angle). The interfacial tension between the molten wax and aqueous glycerol solution was measured by an optical tensiometer (Attention Theta, Biolin Scientific), which can measure the interfacial tension in the range of 0.01–1000 mN/m at a resolution of 0.001 mN/m. Morphology of solidified wax microparticles was characterized by a field emission scanning electron microscope (Quanta 250 FEG, FEI) at low energy intensity of 1.5 kV to avoid melting the wax sample. The density of wax was inferred to be 865 kg/m^3 from the weight of a known volume.

B. Experimental procedures

Our experimental platform is divided into two processes: the formation of wax microdroplets using a flow-focusing microchannel and wax microdroplet impingement on an immiscible liquid interface (see Figure 1). A microfluidic device was fabricated using the soft lithography technique. The replica was fabricated by using a silicon wafer through photolithography with negative photoresist (SU-8, Microchem). We used two different sized flow-focusing microfluidic devices with the orifice dimensions of $70\text{ }\mu\text{m} \times 80\text{ }\mu\text{m}$ and $100\text{ }\mu\text{m} \times 170\text{ }\mu\text{m}$ in width and height. The base and curing agents of polydimethylsiloxane (PDMS) (10:1, Sylgard 184, Dow Corning) were thoroughly mixed and degassed in a vacuum chamber for 30 min. The mixture was poured onto the silicon wafer and cured in an oven at 60°C for 6 h. The cured PDMS was peeled off and bonded onto the glass slide with a plasma cleaner (PDC-001, Harrick Plasma) at 300 mTorr for 3 min. A polyimide etched heating film (FSHH-P1-100-1-B, BioLab, Singapore)

TABLE II. Physical properties of the wax sample at $10^\circ\text{C}/\text{min}$ from 40 to 75°C .

Heat capacity, C_p [kJ/kg K]	1.71
Thermal conductivity, k [W/mK]	0.15
Enthalpy of crystallization, L [kJ/kg]	18.51
Phase transition temperature, T_f [$^\circ\text{C}$]	45.93

provides reliable heat distribution and optical transparency. A voltage ranging from 10 to 20 V was applied by a power supply (Keithley 2000) to control the temperature of the heating film. The temperature of the heating film and the voltage of the power supply were calibrated by a thermometer. The heating film was taped at the glass substrate of the microfluidic device to provide uniform heating of the device, with temperature ranging from 50 to 76 °C to ensure the wax maintaining its molten state inside the microdevice, yet enabling clear optical access to observe the formation of molten wax microdroplets at the orifice, as the microfluidic device was placed on an inverted optical microscope. The flow rate was set to 0.1 ml/h and 1 ml/h for the dispersed phase (molten wax) and the continuous phase (20 wt. % aqueous glycerol solution), respectively. Fluid motion was recorded with a high speed camera (Phantom Miro 310, Vision Research) and the wax microdroplet diameters were measured by ImageJ software. Once the molten wax microdroplets were generated inside the microfluidic device, they were extruded from an outlet and detached by their own weight, before impacting a cooling bath liquid. The molten wax microdroplet is assumed to be homogeneous without any phase change before impact since the wax emulsion is surrounded by the hot aqueous continuous phase, maintaining its molten state. An aqueous glycerol bath was placed beneath the outlet tube in a circular glass beaker and the release height between the tip of the outlet tube and the liquid surface was varied (Figure 1). The viscosity and density of the collecting bath fluid were adjusted by the amount of glycerol added to the aqueous solution. The temperature of the bath fluid was also varied from 8 to 48 °C to investigate the thermal effect on the solidification process of the wax microdroplet.

IV. RESULTS AND DISCUSSIONS

A. Molten wax microdroplet generation

In the flow-focusing region of the device, the molten wax phase periodically breaks into discrete droplets under certain flow rate combinations of the two phases. The droplet formation process is mainly governed by the flow rate ratio, viscosity ratio, and the capillary number ($Ca = \eta_0 V_0 / \sigma_i$), where η_0 is the dynamic zero shear viscosity of the continuous phase, V_0 is the average velocity of the continuous phase at the orifice, and σ_i is the interfacial tension between the dispersed and continuous phases.⁴² Generally, droplet diameters are proportional to the ratio between the interfacial tension and the viscous force exerted from the continuous phase. The first investigation on the droplet diameter dependence with respect to shear rate and surface tension was reported by Taylor,⁴⁷ in which he studied hydrodynamic equations of a spherical drop in a shearing fluid, and concluded that the droplet diameter could be estimated by the balance between the Laplace pressure and shear force, $D \propto \sigma_i / (\eta_0 \dot{\gamma})$. This equation can be normalized to investigate temperature dependent parameters by $D^* = D/D_0$, $\sigma^* = \sigma/\sigma_0$, and $\eta^* = \eta/\eta_0$. In our study, the interfacial tension and the viscosity of the continuous phase are normalized by their nominal values at reference temperature of 52 °C, $\sigma_0 = 11.3$ mN/m and $\eta_0 = 0.0012$ Pa s. The temperature dependence of the dimensionless droplet diameter can be then expressed as⁴⁰

$$D^* \propto \frac{1}{Ca_0} \frac{\sigma^*(\Delta T)}{\eta^*(\Delta T)}, \quad (6)$$

where $\Delta T = T - T_0$ is the temperature difference between instantaneous and reference temperatures, $Ca_0 = V_0 \eta_0 / \sigma_0$ is the capillary number at the reference temperature, and σ^* and η^* are interfacial tension and viscosity functions of the temperature difference ΔT . To simplify the analysis we only considered the correlation between D^* and σ^*/η^* by using the experimental results.

Figures 2(a) and 2(b) show snapshots of molten wax microdroplets formed at 52 °C and 66 °C in the flow-focusing microchannel, representing temperature dependency on droplet diameters. We used the dynamic viscosity of the continuous phase fluid and the interfacial tension between the molten wax solution and the continuous fluid to estimate the molten wax droplet diameter (Figures 3(a) and 3(b)). For the continuous phase, the shear viscosity variation with

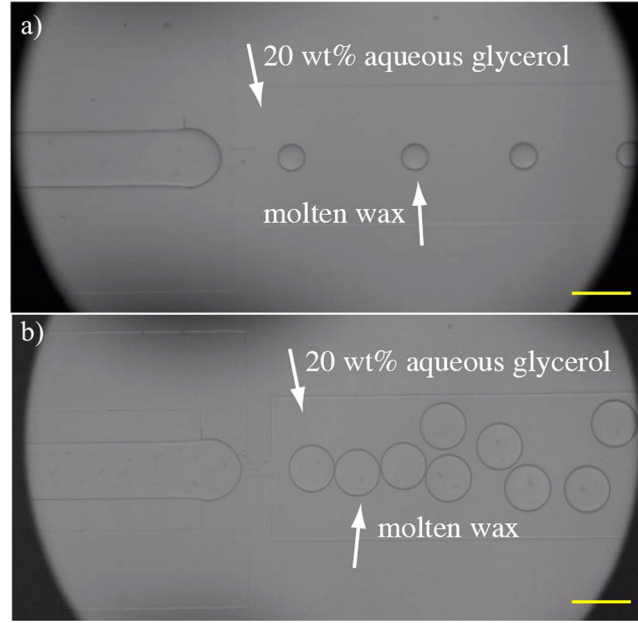


FIG. 2. Wax microdroplet generation inside a flow-focusing channel: (a) $T = 52^\circ\text{C}$ and (b) $T = 66^\circ\text{C}$. The continuous phase flow rate $Q_c = 1$ ml/h and the dispersed phase flow rate $Q_d = 0.1$ ml/h. The scale bar is $200\ \mu\text{m}$.

temperature has been reported to follow an exponential function. Regarding the interfacial tension between two phases, it typically follows a power law trend from existing literature. However, Nguyen *et al.*⁴⁰ observed an exponential decay of interfacial tension with respect to temperature when the temperature variation was less than 50°C . Similarly, from our experimental measurements, the normalized interfacial tension and viscosity yield the best curve fit at $\sigma^* = \exp(0.007\Delta T)$ and $\eta^* = \exp(-0.019\Delta T)$, respectively. The solid line represents the exponential curve fitting with respect to temperature difference ΔT . The dimensionless droplet diameter can now be represented as $D^* \propto \sigma^*/\eta^* \propto \exp(0.026\Delta T)$, displaying that the diameter of molten wax droplet increases with increasing temperature difference. The droplet diameters formed at two different orifice sized flow-focusing channels ($70\ \mu\text{m} \times 80\ \mu\text{m}$ and $100\ \mu\text{m} \times 170\ \mu\text{m}$ in width and height) were measured by imageJ software and normalized by the initial diameter of the molten wax droplet at 52°C (Figure 3(b)). The normalized droplet diameters increased with increasing temperature difference for 2 different sized flow-focusing microchannels. The analytical estimation obtained from Equation (6) also exhibits a typical trend that the

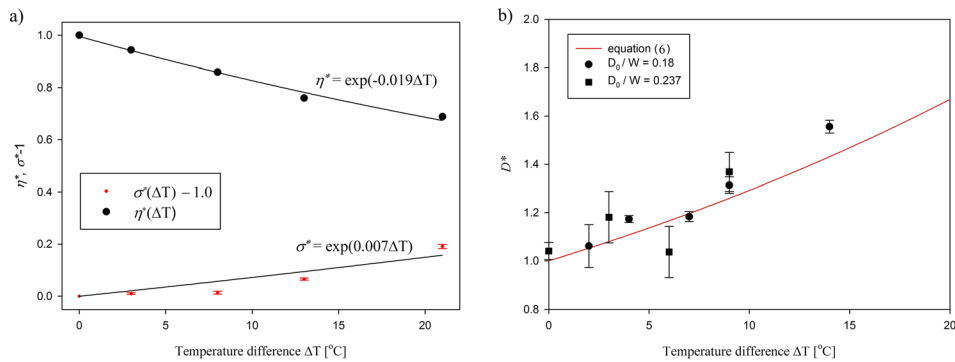


FIG. 3. (a) Normalized viscosity of the continuous phase and normalized interfacial tension between dispersed and continuous phases. The interfacial tension and the viscosity are normalized by their nominal values at 52°C , $\sigma_0 = 11.3$ mN/m and $\eta_0 = 0.0012$ Pa s. The solid lines are the exponential fitting curves. (b) Normalized droplet diameters as a function of temperature. The droplet diameters are normalized by their nominal values at 52°C .

droplet diameter increases with increasing temperature, which shows a reasonable agreement with the experimental data. Some discrepancy does occur at larger temperature differences, which is possibly due to the fact that Equation (6) does not consider the hydrodynamic resistance of droplets in rectangular channels. Furthermore, the temperature gradient derived from the heat source from the bottom of the channel may cause asymmetric heat transfer, leading to a non-uniform temperature field in the microchannel.

B. Droplet impact

After the continuous phase (gray in Figure 4) encapsulates the molten wax (red in Figure 4) droplets, it travels downstream in the microchannel through the outlet. Upon release, the impinging continuous droplet containing the molten wax drop would break the target air–bath (blue in Figure 4(b)) interface with instantaneous deformation. The continuous phase solution in the microchannel is 20 wt. % aqueous glycerol solution mixed with 0.025 wt. % SDS while the bath liquid consists of different amount of glycerol (0, 20, 40, 60, and 80 wt. %) mixed with DI water and 0.025 wt. % SDS. The molten wax droplets are released after the impact toward the bottom of the liquid bath by inertia, and eventually bounce back to the liquid interface due to the fact that the wax droplets are lighter than the bath liquid (see the illustration in Figure 4).

During the impact of the molten wax microdroplet onto the liquid interface, rapid heat transfer occurs between the droplet and the surrounding liquid, leading to the solidification of the molten wax microdroplet. We previously studied the deformation and solidification process of millimeter sized molten wax drops impacting an immiscible liquid interface.³⁶ The deformation of the millimeter sized wax drops was determined by the competition among the inertial, viscous, interfacial, and thermal forces. Mushroom, ellipsoid, disc, and flake-like morphologies were controllably obtained by varying the interfacial, inertial, viscous, and thermal effects. In the millimeter scale case, the initial inertial driven spreading and the residual inertia led to more significant deformation of the molten wax droplet during the impact. In this study, however, the dispersed phase of molten wax first broke into discrete wax microdroplets (red in Fig. 4(a)) at the flow-focusing region in the microchannel. As it traveled downstream and reached the exit tubing, the dripping continuous phase formed droplets (in gray) with encapsulated wax droplets (in red, Fig. 4(b)), acting as a buffer layer to reduce the impact energy upon striking the immiscible liquid interface (illustrated in Figure 9). Therefore, the inertial effect of the wax microdroplets is much smaller than that of the millimeter sized wax drops. The Weber number for the molten wax microdroplet system is only on the order of 10^{-3} – 10^{-1} , in comparison to 10^1 – 10^3 of the millimeter sized wax drops. The Weber number is defined as $We = (\rho_b V_0^2 D) / \sigma_i$, in which ρ_b , V_0 , D , σ_i are the density of the bath, initial impact velocity, diameter of the molten wax droplets, and the interfacial tension between the molten wax and bath fluid. In the microdroplet impact case, the inertial effect is negligible and the viscous and thermal effects become more dominant over the inertial force during the simultaneous deformation and solidification

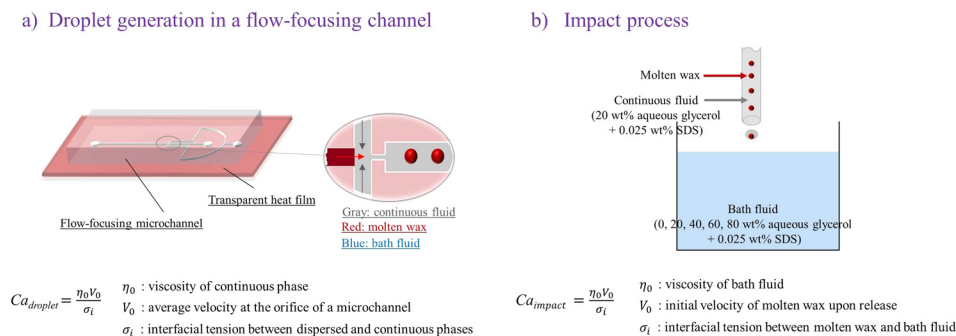


FIG. 4. Different parameters for calculating the Capillary numbers during: (a) emulsion production in a flow-focusing channel and (b) droplet impact process on the cooling bath fluid.

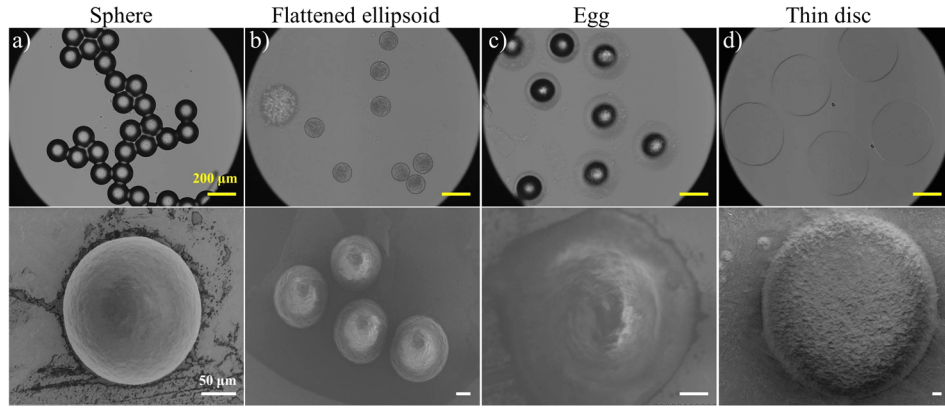


FIG. 5. Four morphologies of wax microparticles observed by optical microscopy (top panel) and scanning electron microscopy images at low energy intensity of 1.5 kV to avoid melting the wax sample (bottom panel), formed after molten microdroplets impinging on an immiscible cooling liquid: (a) sphere; (b) flattened ellipsoid; (c) egg; and (d) thin disc. The yellow and white scale bars represent 200 μm and 50 μm , respectively.

processes of wax microdroplets. The experimental results show four different solidified wax microparticle shapes after impact: sphere, flattened ellipsoid, egg, and thin disc (Figure 5).

The cursory phase diagram represents the predominant shapes that are generated within the range of dimensionless Stefan and Capillary numbers (Figures 6(a) and 6(b)), from microdroplet and millimeter size droplets, showing distinguished differences. The capillary number here is calculated differently from the value in the microchannel (see Figure 4). It is defined as $Ca = \eta_0 V_0 / \sigma_i$, where η_0 is the dynamic zero shear viscosity of the bath fluid, V_0 is the impact velocity of the molten droplet upon release, and σ_i is the interfacial tension between the molten wax and the bath fluid. The dashed lines denote the boundary of particle shape transition. We used the same raw data from our recent studies in macroscale³⁶ and re-analyzed them with a logarithmic x-axis scale in Ca for side-by-side comparison of micron versus millimeter size cases.

For the millimeter sized wax drops, the spreading of molten wax was enhanced with increasing Ca , promoting mushrooms and flake-like shapes ($Ca > 0.5$). Spherical particles did not emerge in the Ca and St phase diagram for the millimeter sized wax droplets (Figure 6(b)). In contrast, spherical micron sized wax particles formed at higher St ($St > 5$) (see Figure 6(b)) because the deformation of the molten wax microdroplets was hindered by the rapid crystallization as St increased. At lower capillary numbers ($0.03 < Ca < 0.5$), less deformable shapes (e.g., spheres or eggs) were favorably generated followed by thin discs. Within $0.1 < Ca < 1.0$, lower St number implied slower crystallization, providing more time for deformation to form thin discs, when compared to higher St for the spherical morphology. For higher capillary numbers ($Ca > 1$), the spreading of the molten wax was hindered by more viscous bath liquid, promoting flattened ellipsoid particles. The morphological difference between wax microparticles and

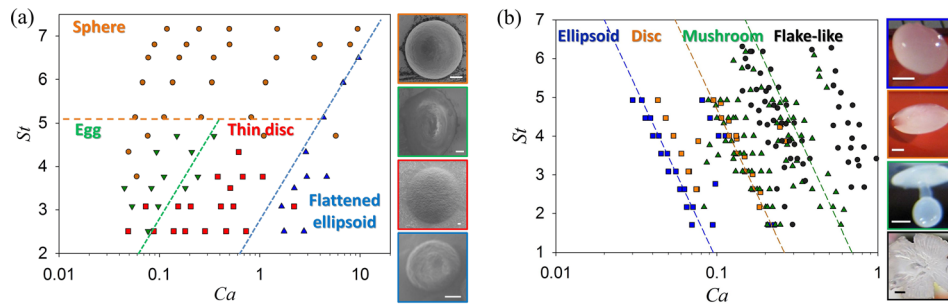


FIG. 6. Cursory phase diagram of wax particle morphologies (a) in micron size (the scale bar is 50 μm); (b) in millimeter size (the scale bar is 1 mm), formed under different Stefan number and Capillary number. The dashed lines represent the shape transition.

millimeter sized particles at high Ca is associated with the influence from the buffer layer from the continuous phase in the microchannel, hence reducing the impact energy significantly during the droplet impact process, forming less deformed wax particles. We also observed opposite trend of slopes in the phase diagram for the micro- versus millimeter-sized particles, which is potentially due to the dominance of thermal effect over the inertial effect as the microdroplets impact on the cold bath fluid. This cursory phase diagram provides a baseline for investigating and understanding the kinematics, heat transfer, and crystallization behaviors of the molten wax droplets upon impacting an immiscible liquid.

The deformation process of molten wax microdroplets is complicated, affected by intrinsic material properties of molten wax and bath solutions, droplet velocity, heat transfer between the molten wax droplet and bath liquid, and crystallization of the molten wax droplet. Here, we first investigate the motion of droplets through an immiscible fluid with thermal effects. We consider the following simplified situation: a molten wax drop of mass m_p moves through an immiscible fluid under the action of gravitational (\tilde{F}_g), drag (\tilde{F}_d), and buoyancy (\tilde{F}_b) forces. Using the equation of motion of a particle falling in a liquid bath by integrating the force balance on the particle, $m_p \tilde{a} = \tilde{F}_g + \tilde{F}_d + \tilde{F}_b$. The drag force acting on the wax particle is assumed to be a Stokes drag since the Reynolds number of the moving wax particle is around 0.1. We then solved the equation of motion of the particle to investigate the terminal velocity of the wax particle with thermal effect by changing the viscosity and density of the bath liquid. The equation of motion is represented as

$$\frac{d\tilde{V}}{dt} = \frac{\rho_p - \rho_b}{\rho_p} \tilde{g} + \frac{6\pi\eta_b D \tilde{V}}{m_p}, \quad (7)$$

where D is the diameter of the wax droplet, the subscripts b and p stand for bath fluid and wax particle, respectively. \tilde{V} is the relative velocity between the wax particle and its surrounding fluid. Since the liquid bath is at rest, \tilde{V} is essentially the same as the velocity of the wax particle.

In this falling body system, the drag force increases with the velocity of the droplet quickly reaching a constant terminal velocity, which can be used to estimate the kinetic energy during the wax deformation.^{48,49} The Ohnesorge number (Oh) represents the importance of the viscous force relative to interfacial tension and inertial forces, expressed by $Oh = \nu \rho_b / (\rho_b D \sigma_i)^{1/2}$, where ν and ρ_b are the kinematic viscosity and density of the bath fluid, D is the diameter of the droplet, and σ_i is the interfacial tension between the bath fluid and the molten wax. Chan and his coworkers used Ohnesorge number (Oh) to examine the relationship between the processing variables and the shape and size of alginate microbeads when alginate microbeads were cross-linked through an extrusion-dripping method, showing the morphological transition at a critical Ohnesorge number ($Oh > 0.24$).⁴⁸ In our study, the Ohnesorge number was plotted against the dimensionless velocity V_T/V_0 while varying St numbers to capture the competing viscous and inertia effects during the droplet impact process (see Figure 7(a)). V_0 is the initial velocity of the continuous phase droplet (glycerol/water containing the molten wax droplet) upon release. The terminal velocity V_T is the velocity at which the drag force balances out the gravitational and buoyancy forces. We show that normalized terminal velocity V_T/V_0 decreases rapidly when $Oh < 0.2$ and reaches a plateau region over $Oh > 0.2$ (Figure 7(a)). That is, the impact energy is high for less viscous solutions ($Oh < 0.2$), which yields more deformed wax particles. Moreover, the thermal effect described by the Stefan number (St) has little effect on V_T/V_0 at higher Oh . As the bath fluid becomes more viscous, the thermal effect becomes less important, resulting in less deformed particles. These observations are in good agreement with experimental results illustrated in the phase diagram at high Ca (Figure 6(a)).

The deformation process of the molten wax droplet is also affected by the combination of buoyancy, gravity, and interfacial tension forces, which are represented by the Bond number ($Bo = (\rho_b - \rho_p)gD^2/4\sigma_i$).⁴⁹ Since the thermal effect is important in our system due to the temperature difference between the molten wax droplet and the cooling bath liquid, V_T/V_0 shows

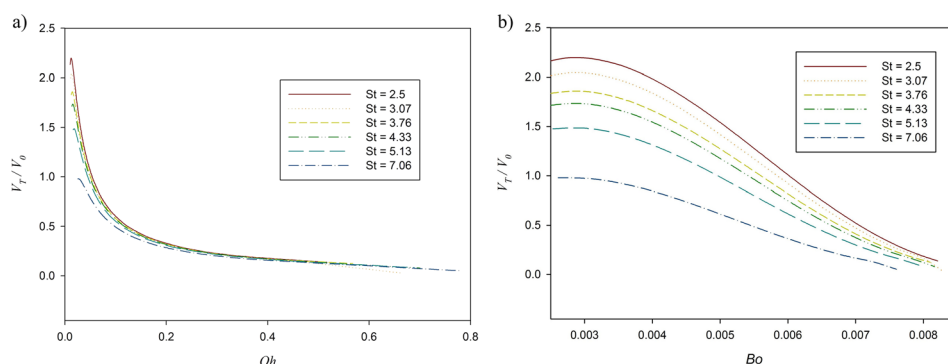


FIG. 7. Dimensionless velocity profile as a function of (a) the Ohnesorge number; and (b) the Bond number while varying Stefan numbers.

larger variation at low Bo with respect to St than the values at high Bo (Figure 7(b)). Furthermore, V_T/V_0 decays to almost zero when Bo reaches 0.008, which demonstrates that the gravitational and buoyancy forces are less dominant than the interfacial tension force since the size of the molten wax droplet is only hundreds of micrometers. Therefore, it is reasonable to relate the final wax morphologies with the Capillary number Ca which represents the viscous and interfacial forces along with the Stefan number St . Note that V_T/V_0 decreases with increasing St in both Bo and Oh plots (Figures 7(a) and 7(b)), indicating that higher St numbers suppressed droplet deformation, evidenced by our experimental results (Figure 6(a)).

C. Crystallization of molten wax microdroplet

During impact, the deformation of a molten wax microdroplet is not only determined by the kinematics of the particle but also associated with its crystallization process. As the molten wax cools down below its phase transition temperature, the wax crystals precipitate and form an interlocked three-dimensional crystal network,⁵⁰ causing continuous crystallization from the surface to the core. Early studies of droplet solidification after impinging on a cooling liquid were mainly motivated by biopreservation, because the vitrification is regarded as the only possible way to cryopreserve human cells and tissues (e.g., oocytes and brain tissue).^{51,52} Crystallization refers to the process of formation of a solid crystal precipitating from its molten state while vitrification is the transformation of a substance into glassy state due to extremely rapid cooling. Once the temperature of microdroplets reaches its freezing point, solidification (crystallization or vitrification) takes place, depending on the cooling rate, nucleation site, and thermal properties of the material.^{52–55} Figure 8(a) shows the molten wax microdroplets

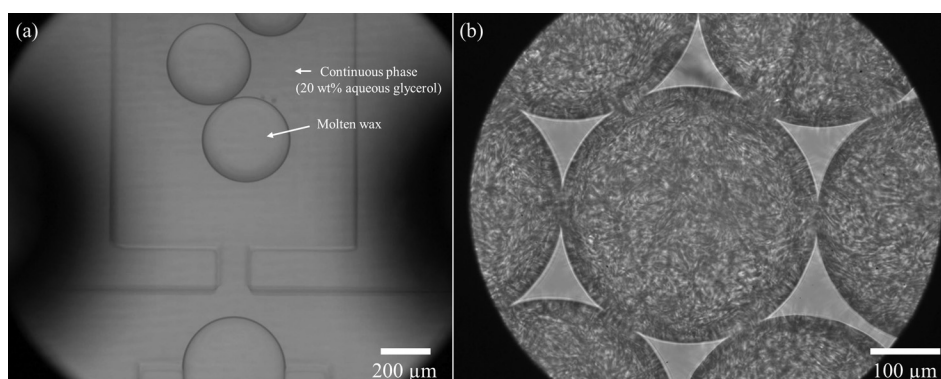


FIG. 8. (a) Molten wax droplets are generated in a flow-focusing microchannel at 66 °C. The flow rate for the continuous phase (20 wt. % aqueous glycerol solution) is $Q_c = 1$ ml/h, and $Q_d = 0.1$ ml/h for the dispersed phase (molten wax). (b) Crystallized wax microparticles after cooling at 23 °C observed by an optical microscope.

produced in a droplet microfluidic device at 66 °C, with solid wax microparticles exhibiting distinct crystallization structures after reaching 23 °C (Figure 8(b)), which demonstrates that the wax microparticles are crystallized during the cooling process.

The theoretical estimation for the kinetics of isothermal crystallization was earlier proposed by Avrami.⁵⁶ Non-isothermal crystallization models with different crystallization temperatures and cooling rates were extensively studied by Nakamura⁵⁷ and Boutron.⁵⁸ The non-isothermal kinetics model proposed by Boutron considers both the growth of spherical crystals and the retarded speed of the ice front, as shown below:⁵⁸

$$\frac{d\chi}{dt} = k_a \chi^{2/3} (1 - \chi) (T_f - T_s) \exp(-Q/RT_s), \quad (8)$$

where χ is the degree of crystallization ($0 \leq \chi \leq 1$), Q (J/mol) is the activation energy, T_f (K) is the onset temperature of crystallization, R (J/mol K) is the gas constant, T_s (K) is the temperature at the surface of the wax droplet, and k_a (1/s K) is the characteristic constant related to the number of nuclei in the wax.⁵⁹ The crystallization process due to heat transfer is governed by both heat convection and heat conduction between the molten wax droplet and the bath liquid. The dimensionless heat transfer equation is expressed as

$$\frac{\partial T^*(r^*, t^*)}{\partial t^*} + \tilde{V}^*(r^*, t^*) \cdot \nabla T^*(r^*, t^*) = \nabla \cdot (\nabla T^*(r^*, t^*)) + \frac{1}{St} \frac{\partial \chi}{\partial t^*}, \quad (9)$$

in which ∇ is the differential vector operator, $T^* = (T - T_\infty)/(T_i - T_\infty)$ is the dimensionless temperature in which T_i is the initial temperature of the droplet surface and T_∞ is the temperature of the surrounding bath liquid, $\tilde{V}^* = (V_r/V_0)\tilde{e}_r$ is the dimensionless velocity in which V_0 is the initial droplet velocity, V_r is the radial velocity of the wax droplet, $t^* = \alpha t/D^2$ is the dimensionless time (same as the Fourier number Fo) in which D is the droplet diameter, $\alpha = k/(\rho C_p)$ is the thermal diffusivity (can be calculated from the thermal conductivity, density, and heat capacity for the molten wax listed in Table II).

The molten wax microdroplet crystallization system consists of three domains: molten wax, buffer layer, and the surrounding bath liquid (Figure 9). By solving two coupled partial differential equations (PDEs) (Eqs. (8) and (9)), the temperature profile at the surface of the molten wax droplet ($T^*(1, t^*) = T_s^*(t^*)$) with respect to time is updated to solve the non-isothermal crystallization equation. In our case, the heat convection is not negligible due to the fact that the Peclet number, $Pe = DV_0/\alpha = 14.79$, is greater than unity when the wax microdroplet initially impacts an immiscible liquid. By using the dimensionless parameters (i.e., the Stefan

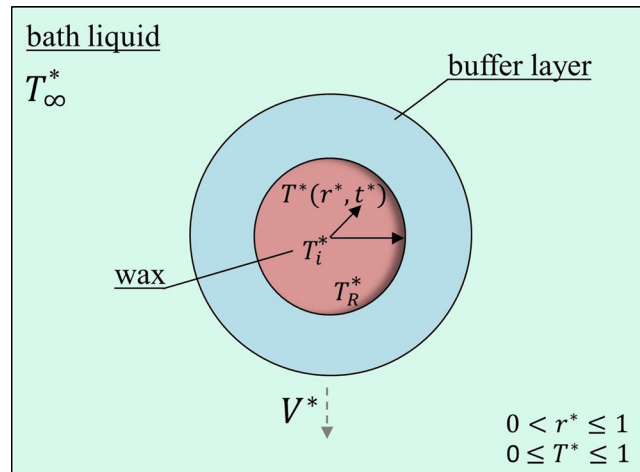


FIG. 9. Schematics of a molten wax microdroplet cooling in an aqueous solution, showing all the key temperature parameters.

number and the Fourier number), we analyzed the dimensionless temperature on the surface of the droplet and the degree of crystallization in the wax phase (Figures 10(a) and 10(b)). Typically, the surface temperature of the droplet decreases rapidly initially and then reaches a plateau when the temperature of the droplet and the surrounding medium reaches an equilibrium (inset in Figure 10(a)). It is noted that $T_s^* = T^*(1, t^*)$ profiles show similar trends along Fo with varying St , giving a general master curve of thermal equilibrium for the molten wax droplet and its surrounding medium with certain thermal properties of materials (Figure 10(a)). In particular, we found that the degree of crystallization of wax droplets increased with an increase in St and Fo (Figure 10(b)). At the highest $St = 7.06$, the degree of crystallization of the molten wax rapidly reached a plateau value $\chi \sim 1.0$ at $Fo = 10$, which represents the complete crystallization that is different from the lower St trends. For lower St , the heat transfer rate between the bath liquid and molten wax is smaller than that of high St , resulting in a slower crystallization rate. Our results reveal that the crystallization process occurs rapidly at large temperature difference, so that the deformation of molten wax droplet is hindered by the fast crystallization. This theoretical prediction is in good agreement with the experimental

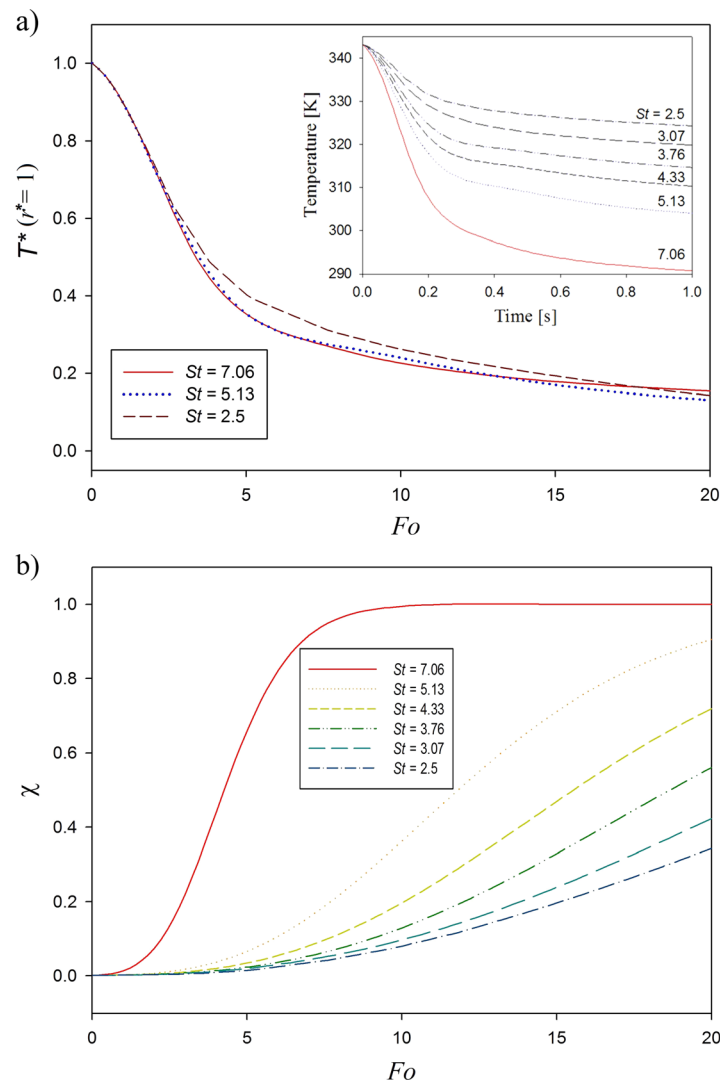


FIG. 10. Change in temperature and degree of crystallization as a function of time. (a) Plot of the dimensionless surface temperature of the molten droplet versus the Fourier number by varying the Stefan number. An inset graph represents the dimensional plot of temperature with respect to time. (b) Plot of the dimensionless crystallinity versus the Fourier number by varying the Stefan number.

results shown in the phase diagram (Figure 6). The wax particles are prone to form spherical shape rather than egg-shaped, thin disc-shaped, and flattened ellipsoid-shaped when $St > 5$. The deformed molten wax droplets are easier to form at lower St (even at high Fo), see Figure 10(b). In short, the deformation of wax droplets impinging on a cooling immiscible liquid was investigated by analyzing the droplet motion, heat transfer, and crystallization of wax microdroplets. The deformation process of the molten microdroplet is complex, and many physical aspects should simultaneously be considered. Our ongoing effort is to solve the droplet impact problem, coupled with the crystallization process numerically with a moving boundary interface by considering deformation of the wax drop upon impact.

V. CONCLUSION

With the aid of a microfluidic platform, molten wax microdroplets were successfully generated in a flow-focusing microchannel. Wax microdroplet diameters formed in the microchannel were controlled by the temperature and could be estimated with respect to the molten wax viscosity and interfacial tension between the molten wax and the aqueous solution. The droplet motion, heat transfer, and crystallization of molten wax microdroplets were analyzed to investigate the deformation process of molten wax microdroplets impinging on an immiscible interface by using various dimensionless parameters. Sphere, egg-shaped, thin disc-shaped, and flattened ellipsoid-shaped morphologies were controllably generated by varying the viscous and thermal effects, and a cursory phase diagram was depicted. The viscous and thermal effects were found to be more dominant over the gravitational and buoyancy effects, promoting morphologies different from those observed in the millimeter sized molten wax drops. The temperature and the degree of crystallization of the wax microdroplets were examined with respect to time by varying the temperature difference between the wax microdroplets and the aqueous bath liquid. The droplet deformation was hindered by fast crystallization due to heat transfer between the wax droplets and the surrounding bath liquid. These theoretical and experimental studies are expected to provide in-depth insight into the general deformation and crystallization behavior, and morphological manipulations of soft materials such as droplets, droplet compounds, and cells impinging on an immiscible liquid interface.

ACKNOWLEDGMENTS

We gratefully acknowledge support from the OIST Graduate University with subsidy funding from the Cabinet Office, Government of Japan.

- ¹S. L. Anna, N. Bontoux, and H. A. Stone, *Appl. Phys. Lett.* **82**, 364–366 (2003).
- ²P. Garstecki, M. J. Fuerstman, H. A. Stone, and G. M. Whitesides, *Lab Chip* **6**, 437–446 (2006).
- ³Y. C. Tan, V. Cristini, and A. P. Lee, *Sensor Actuat. B-Chem.* **114**, 350–356 (2006).
- ⁴S. Y. Teh, R. Lin, L. H. Hung, and A. P. Lee, *Lab Chip* **8**, 198–220 (2008).
- ⁵S. Xu, Z. Nie, M. Seo, P. Lewis, E. Kumacheva, H. A. Stone, P. Garstecki, D. B. Weibel, I. Gitlin, and G. M. Whitesides, *Angew. Chem. Int. Ed.* **44**, 3799–3799 (2005).
- ⁶S. H. Huang, H. S. Khoo, S. Y. ChangChien, and F. G. Tseng, *Microfluid. Nanofluid.* **5**, 459–468 (2008).
- ⁷D. Shalom, R. C. R. Wootton, R. F. Winkle, B. F. Cottam, R. Vilar, A. J. deMello, and C. P. Wilde, *Mater. Lett.* **61**, 1146–1150 (2007).
- ⁸J. Wan, A. Bick, M. Sullivan, and H. A. Stone, *Adv. Mater.* **20**, 3314–3318 (2008).
- ⁹C. H. Chen, A. R. Abate, D. Y. Lee, E. M. Terentjev, and D. A. Weitz, *Adv. Mater.* **21**, 3201–3204 (2009).
- ¹⁰Z. H. Nie, W. Li, M. Seo, S. Q. Xu, and E. Kumacheva, *J. Am. Chem. Soc.* **128**, 9408–9412 (2006).
- ¹¹S. M. Yang, S. H. Kim, J. M. Lim, and G. R. Yi, *J. Mater. Chem.* **18**, 2177–2190 (2008).
- ¹²S. Y. Chou, P. R. Krauss, and P. J. Renstrom, *Science* **272**, 85–87 (1996).
- ¹³J. P. Rolland, B. W. Maynor, L. E. Euliss, A. E. Exner, G. M. Denison, and J. M. DeSimone, *J. Am. Chem. Soc.* **127**, 10096–10100 (2005).
- ¹⁴J. W. Kim, R. J. Larsen, and D. A. Weitz, *Adv. Mater.* **19**, 2005–2009 (2007).
- ¹⁵D. J. Kraft, W. S. Vlugs, C. M. van Kats, A. van Blaaderen, A. Imhof, and W. K. Kegel, *J. Am. Chem. Soc.* **131**, 1182–1186 (2009).
- ¹⁶C. C. Ho, A. Keller, J. A. Odell, and R. H. Ottewill, *Colloid Polym. Sci.* **271**, 469–479 (1993).
- ¹⁷C. C. Ho, A. Keller, J. A. Odell, and R. H. Ottewill, *Polym. Int.* **30**, 207–211 (1993).
- ¹⁸N. Pamme, *Lab Chip* **6**, 24–38 (2006).
- ¹⁹Q. A. Pankhurst, J. Connolly, S. K. Jones, and J. Dobson, *J. Phys. D: Appl. Phys.* **36**, R167–R181 (2003).
- ²⁰M. J. Murray and M. J. Snowden, *Adv. Colloid Interface* **54**, 73–91 (1995).
- ²¹A. H. L. Chow, H. H. Y. Tong, P. Chattopadhyay, and B. Y. Shekunov, *Pharm. Res.* **24**, 411–437 (2007).

- ²²B. Y. Shekunov, P. Chattopadhyay, H. H. Y. Tong, and A. H. L. Chow, *Pharm. Res.* **24**, 203–227 (2007).
- ²³B. Lindlar, M. Boldt, S. Eiden-Assmann, and G. Maret, *Adv. Mater.* **14**, 1656–1658 (2002).
- ²⁴T. Nisisako, T. Torii, T. Takahashi, and Y. Takizawa, *Adv. Mater.* **18**, 1152–1156 (2006).
- ²⁵M. Hoehn, E. Kustermann, J. Blunk, D. Wiedermann, T. Trapp, S. Wecker, M. Focking, H. Arnold, J. Hescheler, B. K. Fleischmann, W. Schwindt, and C. Buhle, *Proc. Natl. Acad. Sci. U.S.A.* **99**, 16267–16272 (2002).
- ²⁶S. Gupta, Q. L. Zhang, T. Emrick, and T. P. Russell, *Nano Lett.* **6**, 2066–2069 (2006).
- ²⁷H. C. Shum, A. R. Abate, D. Lee, A. R. Studart, B. Wang, C. H. Chen, J. Thiele, R. K. Shah, A. Krummel, and D. A. Weitz, *Macromol. Rapid Commun.* **31**, 108–118 (2010).
- ²⁸D. K. Hwang, D. Dendukuri, and P. S. Doyle, *Lab Chip* **8**, 1640–1647 (2008).
- ²⁹T. Fujibayashi and M. Okubo, *Langmuir* **23**, 7958–7962 (2007).
- ³⁰A. Donev, I. Cisse, D. Sachs, E. Variano, F. H. Stillinger, R. Connelly, S. Torquato, and P. M. Chaikin, *Science* **303**, 990–993 (2004).
- ³¹Y. D. Hu, Q. Wang, J. Y. Wang, J. T. Zhu, H. Wang, and Y. J. Yang, *Biomicrofluidics* **6**, 026502 (2012).
- ³²Y. S. Lin, C. H. Yang, Y. Y. Hsu, and C. L. Hsieh, *Electrophoresis* **34**, 425–431 (2013).
- ³³R. G. Craig, J. D. Eick, and F. A. Peyton, *J. Dent. Res.* **44**, 1308–1316 (1965).
- ³⁴R. Kamble, M. Maheshwari, A. Paradkar, and S. Kadam, *AAPS PharmSciTech* **5**(4), 75 (2004).
- ³⁵V. Dodane and V. D. Vilivalam, *Pharm. Sci. Technol.* **1**, 246–253 (1998).
- ³⁶S. N. Beesabathuni, S. E. Lindberg, M. Caggioni, C. Wesner, and A. Q. Shen, *J. Colloid Interface Sci.* **445**, 231–242 (2015).
- ³⁷S. Sugiura, M. Nakajima, and M. Seki, *Langmuir* **18**, 3854–3859 (2002).
- ³⁸A. Gupta and R. Kumar, *Microfluid. Nanofluid.* **8**, 799–812 (2010).
- ³⁹Y. F. Yap, S. H. Tan, N. T. Nguyen, S. M. S. Murshed, T. N. Wong, and L. Yobas, *J. Phys. D: Appl. Phys.* **42**(6) 065503 (2009).
- ⁴⁰N.-T. Nguyen, T.-H. Ting, Y.-F. Yap, T.-N. Wong, J. C.-K. Chai, W.-L. Ong, J. Zhou, S.-H. Tan, and L. Yobas, *Appl. Phys. Lett.* **91**, 084102 (2007).
- ⁴¹Y. Hu, J. Wang, H. Wang, Q. Wang, J. Zhu, and Y. Yang, *Langmuir* **28**, 17186–17192 (2012).
- ⁴²J. D. Tice, A. D. Lyon, and R. F. Ismagilov, *Anal. Chim. Acta* **507**, 73–77 (2004).
- ⁴³M. Jalaal and B. Stoeber, *Soft Matter* **10**, 808–812 (2014).
- ⁴⁴M. Khavari, C. Sun, D. Lohse, and T. Tran, *Soft Matter* **11**, 3298–3303 (2015).
- ⁴⁵S. Pregent, S. Adams, M. F. Butler, and T. A. Waigh, *J. Colloid Interface Sci.* **331**, 163–173 (2009).
- ⁴⁶N. S. Cheng, *Ind. Eng. Chem. Res.* **47**, 3285–3288 (2008).
- ⁴⁷G. I. Taylor, *Proc. R. Soc. London* **146**, 501–523 (1934).
- ⁴⁸E. S. Chan, B. B. Lee, P. Ravindra, and D. Poncelet, *J. Colloid Interface Sci.* **338**, 63–72 (2009).
- ⁴⁹S. Tasoglu, G. Kaynak, A. J. Szeri, U. Demirci, and M. Muradoglu, *Phys. Fluids* **22**, 082103 (2010).
- ⁵⁰F. R. Lupi, D. Gabriele, D. Facciolo, N. Baldino, L. Seta, and B. de Cindio, *Food Res. Int.* **46**, 177–184 (2012).
- ⁵¹G. M. Fahy, D. I. Levy, and S. E. Ali, *Cryobiology* **24**, 196–213 (1987).
- ⁵²Y. S. Song, D. Adler, F. Xu, E. Kayaalp, A. Nureddin, R. M. Anchan, R. L. Maas, and U. Demirci, *Proc. Natl. Acad. Sci. U.S.A.* **107**, 4596–4600 (2010).
- ⁵³A. Bénard and S. G. Advani, *Int. J. Heat Mass Transfer* **38**, 819–832 (1995).
- ⁵⁴C. Le Bot and D. Delaunay, *Mater. Charact.* **59**, 519–527 (2008).
- ⁵⁵H. S. Ren, Y. Wei, T. C. Hua, and J. Zhang, *Cryobiology* **31**, 47–56 (1994).
- ⁵⁶M. Avrami, *J. Chem. Phys.* **7**, 1103 (1939).
- ⁵⁷K. Nakamura, K. Katayama, and T. Amano, *J. Appl. Polym. Sci.* **17**, 1031–1041 (1973).
- ⁵⁸P. Boutron and P. Mehl, *Cryobiology* **27**, 359–377 (1990).
- ⁵⁹P. Boutron, *Cryobiology* **23**, 88–102 (1986).